Application of differential resonant high-energy X-ray diffraction to three-dimensional structure studies of nanosized materials: A case study of Pt–Pd nanoalloy catalysts

Valeri Petkov, Sarvjit Shastri, Jong-Woo Kim, Shiyao Shan, Jin Luo, Jinfang Wu and Chuan-Jian Zhong

Application of differential resonant high-energy X-ray diffraction to three-dimensional structure studies of nanosized materials: A case study of Pt–Pd nanoalloy catalysts

Valeri Petkov,[a]* Sarvjit Shastri,[b] Jong-Woo Kim,[b] Shiyao Shan,[c] Jin Luo,[c] Jinfang Wu[c] and Chuan-Jian Zhong[c]

[a]Department of Physics, Central Michigan University, Mt Pleasant, Michigan 48859, USA, [b]X-ray Science Division, Advanced Photon Source, Argonne National Laboratory, Argonne, Illinois 60439, USA, and [c]Department of Chemistry, State University of New York, Binghamton, New York 13902, USA. *Correspondence e-mail: petko1vg@cmich.edu

Atoms in many of the increasingly complex nanosized materials of interest to science and technology do not necessarily occupy the vertices of Bravais lattices. The atomic scale structure of such materials is difficult to determine by traditional X-ray diffraction and so their functional properties remain difficult to optimize by rational design. Here, the three-dimensional structure of Pt_xPd_{100-x} nanoalloy particles is determined, where $x = 0, 14, 36, 47, 64$ and 100, by a non-traditional technique involving differential resonant high-energy X-ray diffraction experiments conducted at the K edge of Pt and Pd. The technique is coupled with three-dimensional modeling guided by the experimental total and element-specific atomic pair distribution functions. Furthermore, using DFT (density functional theory) calculation based on the positions of atoms in the obtained three-dimensional structure models, the catalytic performance of Pt–Pd particles is explained. Thus, differential resonant high-energy X-ray diffraction is shown to be an excellent tool for three-dimensional structure studies of nanosized materials. The experimental and modeling procedures are described in good detail, to facilitate their wider usage.

1. Introduction

With current science and technology moving to smaller scales, nanosized particles (NPs) are being produced in increasing numbers and explored for an array of useful applications. This is particularly true for metallic NPs finding use in photonics, drug delivery, catalysis and other areas (Cuenya, 2010; Evans *et al.*, 2013; Somorjai, 1994; Link *et al.*, 1999; Tartaj *et al.*, 2003; Lin *et al.*, 2009). Advancing science and technology of metallic NPs though face a major challenge. That is the limited ability to optimize the functionality of the NPs by rational design. It stems from the lack of well established experimental procedures for determining their three-dimensional atomic structure in adequate detail (Billinge & Levin, 2007). The challenge, often referred to as the nanostructure problem, has both technical and fundamental aspects. In particular, the diffraction patterns of metallic NPs show only a few broad, Bragg-like features and a pronounced diffuse component. This renders the sharp-Bragg-peaks-based procedures for determining the three-dimensional atomic structure of bulk metals and alloys technically difficult to apply to metallic NPs. Furthermore, intrinsically like atoms in significant volume fractions of metallic NPs, such as their near-surface region and interior, may not arrange alike (Sun, 2007; Huang *et al.*, 2008; Marks, 1994). Thus, merely because of their high surface area

Pure Pd Pt₁₄Pd₈₆ Pt₃₆Pd₆₄
Pt₄₇Pd₅₃ Pt₆₄Pd₃₆ Pure Pt

electronic reprint
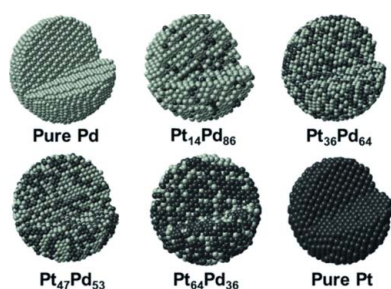
to volume ratio, metallic NPs defy the underlying concept of traditional crystallography that like atoms in metallic materials would occupy like positions in three-dimensional periodic (Bravais) lattices. The approach of considering the diffraction patterns of metallic NPs in terms of atomic pair distribution functions (PDFs) has proven very successful in solving the technical aspect of the nanostructure problem (Egami & Billinge, 2003). The approach of approximating atomic PDFs for metallic NPs, and so their three-dimensional structure, with models embodying replicas of Bravais lattices is undoubtedly very useful (Farrow *et al.*, 2007). However, it does not solve the fundamental aspect of the nanostructure problem. In particular, it is unable to capture the specifics of the atomic arrangement in the near-surface region of metallic NPs that are indeed responsible for many of their unique properties such as, for example, their superb catalytic activity for a number of technologically important reactions (Wang *et al.*, 2000; Tian *et al.*, 2008). Among others, the specifics include the usually significant atomic relaxation and chemical ordering/disordering effects occurring near the surface of metallic NPs. As shown here, the missing knowledge can be obtained by building realistic three-dimensional structure models for the NPs using experimental PDFs sensitive to both the positioning and type of their constituent atoms. As also shown here, the knowledge can provide a sound structural basis for rationalizing functional properties of the NPs that play an important role in practical applications.

By their nature, experimental atomic PDFs for metallic NPs are a one-dimensional representation of their three-dimensional atomic structure. Hence, the amount of information for the three-dimensional structure of metallic NPs carried by a single atomic PDF is hardly enough to accurately determine the former on the basis of the latter alone (Farrow *et al.*, 2011). The general understanding is that an accurate determination of the three-dimensional structure of metallic NPs may require not only a combination of X-ray, neutron and/or electron diffraction experiments but also augmentation of the resulting PDFs with data from other NP structure-sensitive techniques such as extended absorption X-ray fine structure (EXAFS) spectroscopy, electron microscopy, nuclear magnetic resonance and others. In addition, analysis of the PDF and complementary experimental data ought to be integrated with advanced three-dimensional structure modeling techniques (Billinge & Levin, 2007). Here we determine the three-dimensional structure of Pt–Pd nanoalloy catalysts by resonant high-energy X-ray diffraction (HE-XRD) experiments conducted at the K edges of both Pt and Pd. The resulting element-specific atomic PDFs are augmented with data for the size, shape and chemical composition of the catalyst particles obtained by independent inductively coupled plasma optical emission spectroscopy (ICP-OES), high-resolution transmission electron microscopy (HR-TEM), high-angle annular dark-field scanning transmission electron microscopy (HAADF-STEM), energy-dispersive X-ray spectroscopy (EDS) and X-ray photoelectron spectroscopy (XPS) experiments. Three-dimensional structure models for the NPs are built by mol-

ecular dynamics (MD) simulations and refined against the respective total and element-specific PDFs by reverse Monte Carlo (RMC) computations.

Developing clean energy conversion technologies, such as fuel cells, is crucial for satisfying the soaring demand for energy worldwide while keeping the environment clean. At present, the lack of efficient and affordable catalysts for the chemical reactions that drive fuel cells, such as the oxygen reduction reaction (ORR), is a major obstacle on the road to their commercialization. Largely, the obstacle stems from the fact that Pt, which is the best monometallic catalyst for the ORR, is among the world's rarest metals. Studies have indicated that, in addition to involving less Pt, Pt–Pd alloy NPs may well be more active and stable catalysts for the ORR in comparison to pure Pt (Seh *et al.*, 2017; Lu *et al.*, 2013; Quan *et al.*, 2015; Li *et al.*, 2007). While the preparation and catalytic characterization of Pt–Pd alloy NPs have been a subject of numerous studies, the relationship between their catalytic activity and atomic level structure has received much less attention. We clarify the relationship by studying Pt_xPd_{100-x} alloy NPs ($x = 14, 36, 47, 64$), which have shown an unusual evolution of the ORR activity with the bimetallic composition (Wu *et al.*, 2017). Note that following the widely adopted definition, here we use the term 'alloy' to describe any mixture of distinct metallic species, irrespective of the degree of their mixing and way of mixing (Callister, 2007).

2. Experimental

2.1. Sample preparation

Pt–Pd NPs were synthesized using Pt^{II} and Pd^{II} acetylacetonate as metal precursors, and dioctyl ether as a solvent. Oleic acid and oleylamine were used as capping agents, and 1,2-hexadecanediol was used as a reducing agent. The precursors were mixed in pre-desired ratios and heated gradually to 493 K under N_2 atmosphere. The solution was then cooled back to room temperature and Pt–Pd NPs precipitated out by washing and centrifugation. The NPs were deposited on fine carbon powder (XC-72) and activated for catalytic applications by a thermochemical treatment involving heating at 533 K under N_2 atmosphere for 30 min and further heating at 673 K under (15% H_2)–(85% N_2) atmosphere for 2 h. The treatment is necessary to remove the organic molecules capping the NP surface. Pure Pt and Pd NPs were prepared and activated for catalytic applications in a similar manner. More details of the synthesis protocol employed here can be found in Wu *et al.* (2017).

2.2. Determination of the chemical composition, size and shape of Pt–Pd NPs

The chemical composition of Pt–Pd NPs was determined by ICP-OES on a PerkinElmer 2000 DV instrument using a Meinhardt nebulizer coupled to a cyclonic spray chamber. Standards and the unknowns were analyzed several times each resulting in <3% error in the chemical composition. Experi-
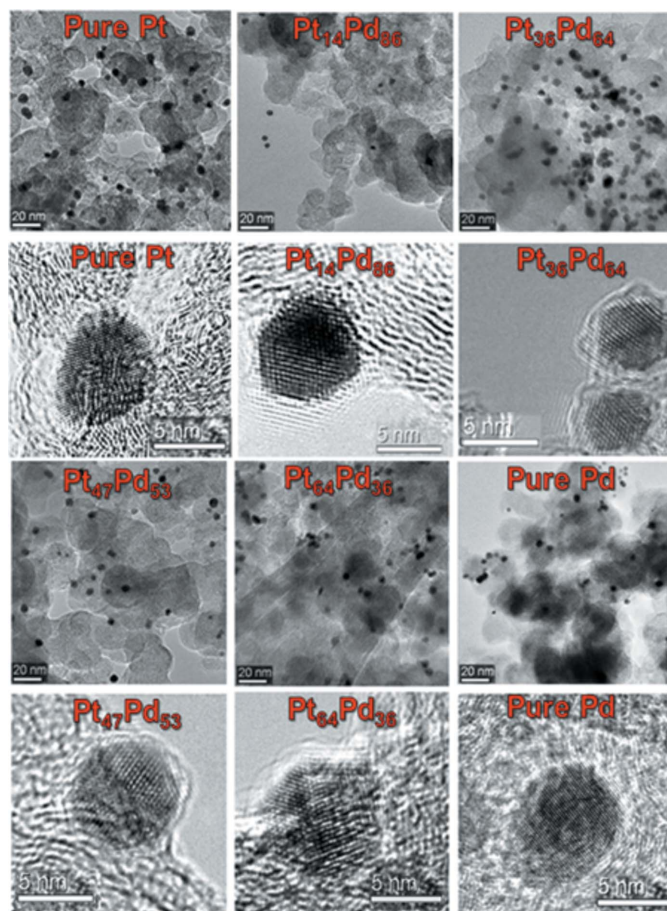
Figure 1
Representative TEM and HR-TEM images of pure Pt, Pd and Pt_xPd_{100-x} alloy NPs (x = 14, 36, 47, 64). The NPs have an average size of approximately 5.3 ($\pm$ 0.5) nm and near-polyhedral shape with round edges. The clearly visible lattice fringes in the HR-TEM images indicate that the NPs possess a good degree of crystallinity. Note that the reported '$\pm$' deviation from the average NP size is the full width at half maximum of a Gaussian-like distribution of sizes extracted from populations of several hundred NPs sampled by different TEM images. The contrast of the scale bars has been enhanced for better visibility.

with a CEOS Hexapole probe corrector and an EDS SDD detector. HAADF-STEM images and elemental maps are shown in Fig. 2. The maps indicate that the NPs are near random alloys. Hence, hereafter, they are referred to as Pt–Pd alloy NPs.

2.3. Differential resonant HE-XRD experiments

The frequently used atomic PDF $G(r)$ is defined as

$$G_{(r)} = 4\pi r[\rho(r) - \rho o], \tag{1}$$

where $\rho(r)$ and ρo = const $\neq 0$ are, respectively, the local and average atomic number density of the studied material, and r is the radial (real-space) distance (Egami & Billinge, 2003; Waseda, 1984; Klug & Alexander, 1974). Typically, a PDF for NPs is obtained by conducting a carefully designed HE-XRD experiment (Petkov, 2008; Petkov & Shastri, 2010), correcting the raw experimental pattern for experimental artifacts (*e.g.* background scattering, sample absorption *etc.*), converting the corrected pattern into absolute electron units, and deriving the so-called structure function, $S(q)$, defined as

$$S(q) = \frac{I^{coh}(q) - [\langle f^2(q) \rangle - \langle f(q) \rangle^2]}{\langle f(q) \rangle^2} = \frac{I^{coh}(q) - \langle f^2(q) \rangle}{\langle f(q) \rangle^2} + 1, \tag{2}$$

where $I^{coh}(q)$ are the coherently scattered intensities extracted from the raw HE-XRD pattern, $f(q)$ is the X-ray atomic scattering factor, q is the magnitude of the wavevector ($q = 4\pi \sin\theta/\lambda$), 2θ is the angle between the incoming and outgoing X-rays, and λ is the wavelength of the X-rays used. The $G(r)$ is then computed by Fourier transforming the $S(q)$, as follows:

$$G(r) = (2/\pi) \int_{q=q_{min}}^{q=q_{max}} q[S(q) - 1] \sin(qr) \, dq, \tag{3}$$

where q_{min} and q_{max} are, respectively, the minimum and maximum wavevector reached with the particular experiment.

mental data showed that the overall chemical composition of Pt–Pd NPs is Pt_xPd_{100-x}, where x = 14, 36, 47, 64.

The size and shape of pure Pt, Pd and Pt–Pd NPs were determined by TEM on a JEM-2200FS instrument operated at 200 kV. Example TEM and HR-TEM images of the NPs are shown in Fig. 1. The images reveal that the NPs have an average size of approximately 5.3 ($\pm$ 0.5) nm and are shaped as polyhedra with round edges. Also, the NPs are seen to possess a good degree of crystallinity.

The chemical pattern of Pt–Pd NPs was investigated by HAADF-STEM and EDS on a JEOL JEM2100F electron microscope operated at 200 kV. The microscope was equipped

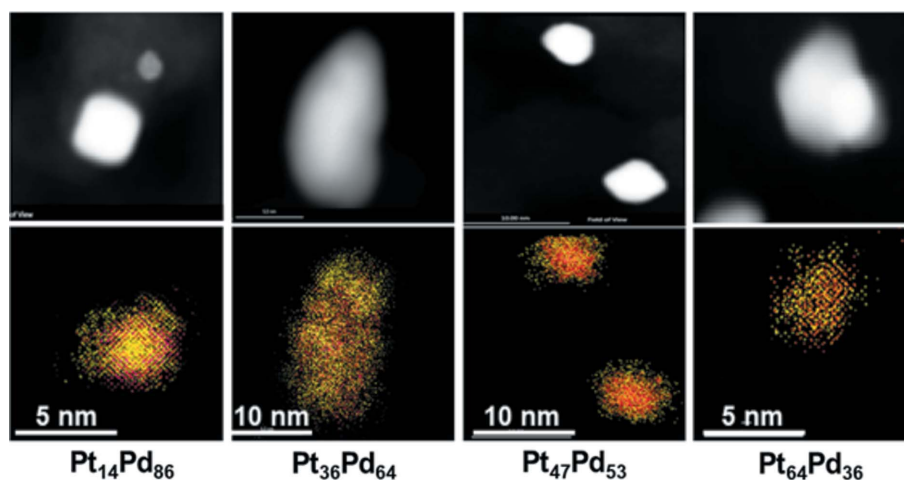**Figure 2**
Representative HAADF-STEM images (first row) and corresponding EDS elemental maps (second row) of Pt_xPd_{100-x} alloy NPs (x = 14, 36, 47, 64). Maps indicate that Pt and Pd species in the NPs are well intermixed together. Pt atoms are in red and Pd atoms are in yellow.

As defined and obtained, the $G(r)$ oscillates about zero and peaks at distances where $\rho(r) > \rho o$, *i.e.* at distances between frequently occurring pairs of atoms in the studied NPs. The area under the peaks is proportional to the number of atomic pairs at those distances. However, despite being informative, an atomic PDF $G(r)$ resulting from a single diffraction experiment on metallic alloy NPs, usually referred to as a total PDF $G(r)$, may not necessarily reveal their atomic level structure in adequate detail. That is because PDF peaks reflecting chemically distinct atomic pairs in the NPs may overlap significantly, rendering the interpretation of experimental PDF data ambiguous. In particular, total PDFs for Pt–Pd alloy NPs reflect chemically distinct Pt–Pt, Pt–Pd and Pd–Pd atomic pairs, *i.e.* they appear as a weighted sum of $G_{Pt–Pt}(r)$, $G_{Pt–Pd}(r)$ and $G_{Pd–Pd}(r)$ partial PDFs. Generally, the sum can be expressed as (Waseda, 1984)

$$G(r) = \sum_{i,j} w_{ij}(q) G_{ij}(r) \qquad (4)$$

where the so-called weighting factors $w_{ij}(q)$ are defined as

$$w_{ij}(q) = c_i c_j \mathrm{Re}\left[\frac{f_i(q)f_j^*}{\langle f(q)\rangle^2}\right]. \qquad (5)$$

Here c_i is the concentration of i-type atomic species (i = Pt, Pd). The non-negligible weighting factors $w_{ij}(q = 0)$ for $G_{Pt–Pt}(r)$, $G_{Pt–Pd}(r)$ and $G_{Pd–Pd}(r)$ partial PDFs for $Pt_xPd_{100−x}$ alloy NPs (x = 14, 36, 47, 64) are summarized in Table S1 (see the supporting information). Owing to the similar size of Pt (2.775 Å) and Pd (2.755 Å) atoms (Pearson, 1972), the partial PDFs are entangled, making it difficult to differentiate between the distinct pairs of atoms in the respective NPs.

To obtain the partial PDFs for Pt–Pd alloy NPs, *i.e.* to obtain diffraction data sensitive to both the positioning and type of atoms constituting the NPs, we conducted resonant HE-XRD experiments at the K edges of both Pt and Pd. The technique has already proven useful in structure studies of materials lacking three-dimensional periodicity at the atomic scale (Fuoss *et al.*, 1981; Waseda, 1984; Kortright & Bienenstock, 1988; Petkov & Shastri, 2010). The experiments were carried out, respectively, using beamline 1-ID and 6-ID-B at the Advanced Photon Source at the Argonne National Laboratory. Samples were sealed in thin-walled glass capillaries with a diameter of 1 mm and measured in transmission geometry using an X-ray beam with a fixed size of 0.5×0.5 mm. An empty glass capillary, carbon powder alone and bulk Pt (polycrystalline powder) were measured separately. The experimental setups were calibrated with a high-purity powder Si standard. Experiments at the K edge of Pt were conduced using X-rays with energy of 78.370 keV (λ = 0.1535 Å) and 78.070 keV (λ = 0.1541 Å). The first energy is 25 eV and the second energy is 325 eV below the K absorption edge of Pt (78.395 keV). X-rays were delivered by a combination of a bent double-Laue monochromator and a four-crystal high-energy resolution monochromator (Shastri, 2004). Scattered X-rays intensities were collected with a solid-state Ge detector coupled to a multi-channel analyzer. A few

energy windows, covering several neighboring channels, were set up to obtain X-ray intensities integrated over specific X-ray energy ranges during the data collection, as exemplified in Figs. 3(*a*) and 3(*b*). The energy windows covered: the coherent intensities only; the coherent, Compton and Pt $K\beta$ fluorescence intensities altogether; the Pt $K\alpha_1$ and $K\alpha_2$ fluorescence; and the total intensities scattered into the Ge detector. The patterns were collected several times scanning from q_{min} of 1 Å^{-1} up to q_{max} of 25 Å^{-1} and then averaged to improve the statistical accuracy. More details of the experimental setup can be found in the supporting information.

Example HE-XRD patterns for $Pt_{14}Pd_{86}$ alloy NPs, one obtained using X-rays with energy of 78.070 keV and the other obtained using X-rays with energy of 78.370 keV, are shown in Fig. 3(*c*). The intensity difference between the patterns is significant [see Fig. 3(*d*)] and largely due to the difference in the X-ray scattering factor of Pt at the two energies. To be more precise, generally, the X-ray atomic scattering factor, $f(q)$, is a function of both the wavevector q and the X-ray energy E, *i.e.*

$$f(q) = f_o(q) + \Delta f'(q,E) + i\Delta f''(q,E), \qquad (6)$$

where $f_o(q)$ is a well known function of q, and $\Delta f'(q,E)$ and $\Delta f''(q,E)$ are the so-called real and imaginary dispersion corrections to $f_o(q)$ (Chantler, 1995). Hence, the stoichiometric average short notations $\langle f(q)^2 \rangle$ and $\langle f(q)\rangle^2$ in equation (2) can be represented as

$$\langle f(q)\rangle^2 = \left[\sum c_i f_i(q,E)\right]^2 = \langle f\rangle\langle f^*\rangle = \langle [f_o(q) + \Delta f']\rangle^2 + \langle \Delta f''\rangle^2 \qquad (7)$$

and

$$\langle f(q)^2\rangle = \sum c_i f_i(q,E)^2 = \langle [f_o(q) + \Delta f']^2\rangle + \langle (\Delta f'')^2\rangle, \qquad (8)$$

where $f^*(q)$ is the complex conjugate of $f(q)$. In practice though, the dependence of dispersion corrections $\Delta f'(q,E)$ and $\Delta f''(q,E)$ on q is very small and so they can be treated as constants for a given energy (Waseda, 1984; Petkov, 2008). Values of the dispersion corrections $\Delta f'(Pd)$ and $\Delta f''(Pd)$ to the $f_o(q)$ of Pd are nearly constant in the 78–79 keV energy range. Hence, in processing the HE-XRD data obtained at the K edge of Pt, we used their well known literature values (Chantler, 1995). For X-ray energies in the vicinity of the K edge of Pt though, values of the dispersion corrections $\Delta f'(Pt)$ and $\Delta f''(Pt)$ to the $f_o(q)$ of Pt, in particular the values of $\Delta f'(Pt)$, are significant. The values were obtained by a three-step procedure. First, the X-ray absorption spectrum of thin Pt foil was measured over an energy range from 76 keV to 81 keV. Second, the resulting data were scaled to match the well known theoretical estimates for $\Delta f''(Pt)$ away from the Pt K edge (Chantler, 1995) and so obtain an energy spectrum of $\Delta f''(Pt)$ in absolute units. Third, $\Delta f'(Pt)$ values were computed from the energy spectrum of $\Delta f''(Pt)$ *via* the Kramers–Kroning relation (Petkov & Shastri, 2010):

$$\Delta f'(E) = \frac{2}{\pi} P \int \frac{E_i f''(E_i)}{E^2 - E_i^2} dE_i, \qquad (9)$$
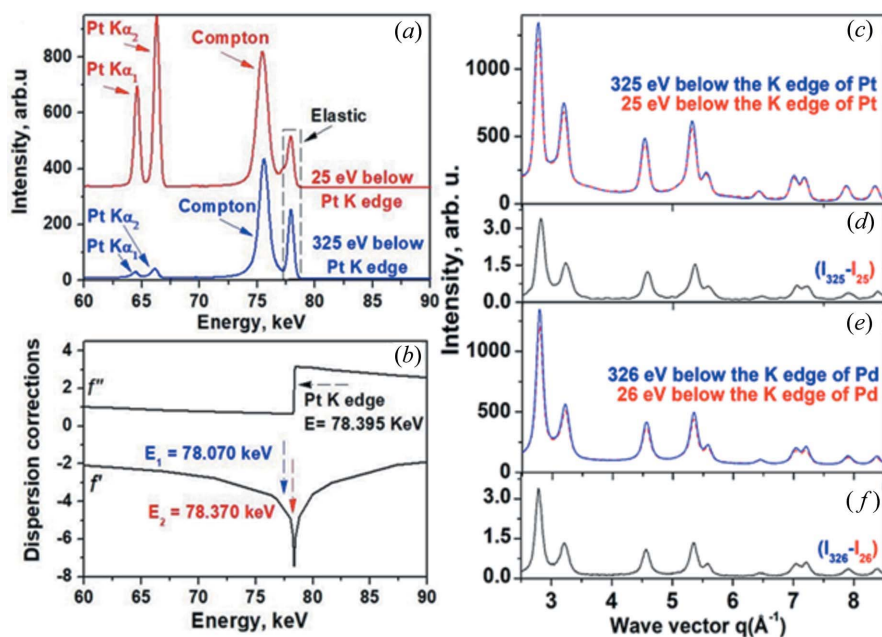
Figure 3
(a) X-ray energy sensitive spectra for $Pt_{14}Pd_{86}$ alloy NPs taken at a fixed diffraction (Bragg) angle of 40°. Spectra are obtained using X-rays with energies of 78.070 keV (blue line) and 78.370 keV (red line). As shown in (b), the first energy is 325 eV below and the second energy is 25 eV below the K absorption edge of Pt (78.395 keV). Elastically and inelastically (Compton) scattered intensities as well as Pt ($K\alpha_1 + K\alpha_2$) fluorescent lines are marked with solid arrows. (b) Energy dependence of the real $\Delta f'$ and imaginary $\Delta f''$ dispersion corrections to the X-ray scattering factor of Pt. $\Delta f'$ was calculated from the measured $\Delta f''$ values via the Kramers–Kroning relation [see equation (9)]. The energies below the K edge of Pt used in the present experiments are marked with vertical dashed arrows. (c) Experimental HE-XRD patterns (low-q part) for $Pt_{14}Pd_{86}$ alloy NPs measured using X-rays with two different energies below the K edge of Pt. The energies are marked with vertical dashed arrows in (b). The patterns include only elastically scattered intensities, i.e. intensities falling into the 'X-ray energy window' outlined with a broken line in (a). The significant intensity difference between the patterns is shown in (d). (e) Experimental HE-XRD patterns (low-q part) for $Pt_{14}Pd_{86}$ alloy NPs measured using X-rays with two different energies (326 and 26 eV) below the K edge of Pd (24.341 keV). The patterns include only elastically scattered intensities obtained as described in the text. The significant intensity difference between the patterns is shown in (f). Note that the energy separation between elastically and inelastically scattered intensities diminishes with the diffraction angle. The inelastically scattered intensities, though, also diminish with the diffraction angle (e.g. see Fig. 1 in Petkov et al., 2000). Therefore, often, a properly set 'X-ray energy window' would eliminate the inelastically scattered intensities from the entire HE-XRD pattern to an adequate extent. Occasionally, residual inelastic intensities at low diffraction angles have to be eliminated analytically, e.g. as described in Ruland (1964).

Si(111) monochromator. Scattered X-rays intensities were collected with an Si PIN diode detector coupled to a multi-channel analyzer allowing discriminating between the scattered X-rays intensities in terms of their energy. By setting 'energy windows' incorporating several neighboring channels of the analyzer, only elastic/coherent intensities scattered from Pt–Pd NPs were obtained. The patterns were collected several times scanning from q_{min} of 1 Å^{-1} up to q_{max} of 25 Å^{-1} and then averaged to improve the statistical accuracy. Example HE-XRD patterns for $Pt_{14}Pd_{86}$ alloy NPs, one obtained using X-rays with an energy of 24.015 keV and another one obtained using X-rays with an energy of 24.315 keV, are shown in Fig. 3(e). The intensity difference between the patterns is significant [see Fig. 3(f)] and is largely due to the difference in the X-ray scattering factor of Pd at the two energies. The respective $\Delta f'(Pd)$ and $\Delta f''(Pd)$ values were obtained following the three-step procedure described above, this time measuring the X-ray absorption spectrum of thin Pd foil across the Pd K edge and matching the resulting data to the well known theoretical estimates for $\Delta f''(Pd)$ away from the edge (Chantler, 1995). The resulting energy spectrum of $\Delta f''(Pd)$ was used to compute the values of $\Delta f'(Pd)$ via equation (9). The values of $\Delta f'(Pd)$ and $\Delta f''(Pd)$ at $E = 24.315$ keV turned out to be −5.72 and 0.54, respectively. At $E = 24.015$ keV the values of $\Delta f'(Pd)$ and $\Delta f''(Pd)$ were, respectively, −2.7 and 0.56. For reference, values of the dispersion corrections to the X-ray scattering factors of Pt and Pd used in the present work are summarized in Table S2 (see the supporting information).

Ideally, structure factors computed from the patterns of Pt–Pd alloy NPs obtained near (~ -25 eV) and below (~ -325 eV) the K edge of Pt and Pd can be combined in a set of equations and the partial $G_{Pt-Pt}(r)$, $G_{Pt-Pd}(r)$ and $G_{Pd-Pd}(r)$ PDFs for the NPs obtained. It has been shown though that such an approach to determining partial PDFs is prone to significant errors (Munro, 1982). Hence, here we employed the so-called differential method for determining element-specific atomic PDFs from resonant HE-XRD data. The advantages of the method, originally referred to as frequency modulated XRD, are discussed in the literature (Shevchik, 1977a,b; Kofalt et al., 1986). The method consists of taking the difference between the coherent parts of HE-XRD data sets obtained at two energies below the absorption edge

where P denotes the Cauchy principal value. The values of $\Delta f'(Pt)$ and $\Delta f''(Pt)$ at $E = 78.370$ keV turned out to be −7.8 and 0.6, respectively. At $E = 78.070$ keV the values were, respectively, −4.1 and 0.62. Total structure functions $S(q)$ [see equation (2)] for Pt–Pd NPs computed using the respective experimental HE-XRD patterns and the values of $\Delta f'(Pt)$ and $\Delta f''(Pt)$ obtained at $E = 78.070$ keV were Fourier transformed [see equation (3)] and the total PDFs $G(r)$ for the NPs obtained. Total PDFs for pure Pt and Pd NPs were obtained in the same way. The higher-r range of the total PDFs for all NPs studied here is shown in Fig. 4(a). An extended range of the PDFs is shown in Fig. 5(a).

Experiments at the K edge of Pd were conducted using X-rays with energies of 24.015 keV (λ = 0.5157 Å) and 24.315 keV (λ = 0.5094 Å). The first energy is 326 eV and the second energy is 26 eV below the K absorption edge of Pd (24.341 keV), respectively. X-rays were delivered by an

of atomic species A in the studied material, $e.g.$ 25 eV and 325 eV below, and computing the so-called differential structure function, $DS(q)_A$, defined as (Serimaa et $al.$, 1995; Waseda, 1984; Petkov & Shastri, 2010)

$$DS(q)_A = \frac{I^{\text{coh}}(q, E_1) - I^{\text{coh}}(q, E_2) - [\langle f^2(E_1) \rangle - \langle f^2(E_2) \rangle]}{\langle f(E_1) \rangle^2 - \langle f(E_2) \rangle^2} + 1.$$

(10)

The corresponding differential atomic PDF, $DG(r)_A$, is derived via a Fourier transformation as follows:

$$DG(r)_A = (2/\pi) \int_{q=q_{\min}}^{q=q_{\max}} q \big[DS(q)_A - 1 \big] \sin(qr) \, dq.$$

(11)

Note that since only the $\Delta f'(E)$ of atomic species A changes significantly, $DG(r)_A$ contains contributions from atomic pairs involving A-type atoms only, $i.e.$

$$DG(r)_A = \sum_i \Delta w_{Ai} G_{Ai}(r)$$

(12)

where

$$\Delta w_{AA} = \frac{c_A^2 [f_A^2(E_1) - f_A^2(E_2)]}{\langle f(E_1) \rangle^2 - \langle f(E_2) \rangle^2} \quad \text{and}$$

$$\Delta w_{A,i \neq A} = \frac{2 c_A c_i \text{Re}\{f_i [f_A^*(E_1) - f_A^*(E_2)]\}}{\langle f(E_1) \rangle^2 - \langle f(E_2) \rangle^2}.$$

(13)

Differential $DG(r)_{\text{Pt}}$ functions for $\text{Pt}_x\text{Pd}_{100-x}$ alloy NPs (x = 14, 36, 47, 64) derived by Fourier transforming the significant intensity difference between their HE-XRD patterns obtained using X-rays with incident energy of 78.070 and 78.370 keV [$e.g.$ see Fig. 3(d)] are shown in Fig. S1(a) (see the supporting information). Differential $DG(r)_{\text{Pd}}$ functions for the NPs derived by Fourier transforming the significant intensity difference between their HE-XRD patterns obtained using X-rays with energy of 24.015 and 24.315 keV [$e.g.$ see Fig. 3(f)] are shown in Fig. S1(b) (see the supporting information). Finally, by using the so-called MIXSCAT approach (Wurden et $al.$, 2010), $G_{\text{Pt-Pt}}(r)$ and $G_{\text{Pd-Pd}}(r)$ partial PDFs for Pt–Pd alloy NPs were derived as follows:

$$G_{\text{Pt-Pt}}(r) = \frac{\text{respective total } G(r)}{w_{\text{Pt-Pt}}} - \frac{\text{respective } DG(r)_{\text{Pd}}}{\Delta w_{\text{Pd}-i}}$$

(14)

and

$$G_{\text{Pd-Pd}}(r) = \frac{\text{respective total } G(r)}{w_{\text{Pd-Pd}}} - \frac{\text{respective } DG(r)_{\text{Pt}}}{\Delta w_{\text{Pt}-i}}.$$

(15)

Here $w_{\text{Pt-Pt}}$ and $w_{\text{Pd-Pd}}$ are computed using equation (5), and $\Delta w_{\text{Pd}-i}$ and $\Delta w_{\text{Pt}-i}$ are computed using equation (13). The resulting partial $G_{\text{Pt-Pt}}(r)$ and $G_{\text{Pd-Pd}}(r)$ PDFs are shown in Fig. 5(c). Note that the MIXSCAT approach is efficient when resonant HE-XRD data sets are measured with the same statistical accuracy, q-space resolution, $q_{\max}$ value and, furthermore, the atomic PDFs appearing in the right-hand side of equation (14) and equation (15) are computed in a similar manner, $e.g.$ with the same Δr step, as done here. In addition,

both the contribution of the individual atomic pair correlations to the HE-XRD data (see Table S1 in the supporting information) and the changes in the X-ray atomic scattering factors, in particular $\Delta f'(E)$ values (see Table S2 in the supporting information), should be significant. Here it is to be stressed that, without affecting accuracy significantly, the seemingly complex equations (2), (5), (7), (8), (10) and (13) can be simplified significantly, $e.g.$, by approximating $f_o(q) \rightarrow f_o(q = 0) \rightarrow Z$; $\Delta f'(E)$ and $\Delta f''(E) \rightarrow 0$ for E away from an X-ray absorption edge (Serimaa et $al.$, 1995; Shevchik, 1977b; Matsubara & Waseda, 1986).

3. General consideration of the total and element-specific PDFs for Pt–Pd NPs with respect to their catalytic properties

The total and partial PDFs obtained by the resonant HE-XRD experiments conducted here reflect characteristic structural features of the large ensemble of Pt–Pd NPs sampled by the synchrotron X-ray beam, including the positioning and type of atoms constituting the NPs. As demonstrated recently, NP ensemble-averaged three-dimensional atomic positions are a very proper basis for not only establishing but also quantifying the structure–function relationship in metallic NPs pursued for catalytic applications. This may not come as a big surprise because the actual catalytic functionality of metallic NPs also appears as an ensemble-averaged quantity (Petkov et $al.$, 2017).

Furthermore, physical peaks in the experimental PDFs for Pt–Pd NPs reflect correlations between Pt and/or Pd atoms, immediate and all farther neighbors, within the sampled NPs. Since surface atoms at the opposite sides of metallic NPs are separated the most, it may be expected that the experimental total PDFs would exhibit physical peaks up to real-space distances commensurate with the average size of the respective NPs, as determined from large populations of NPs sampled by TEM (see Fig. 1). In addition, PDF peaks at these higher-r distances would primarily reflect correlations between atoms in the near-surface region of the NPs and so appear diminished in intensity compared with those in PDFs for the bulk counterpart of the NPs. Indeed this is exactly what the experimental data in Figs. 4(a), 4(b) and 4(c) show. The good agreement between the average NP size determined by TEM and real-space distances at which the physical oscillations in the total PDFs for Pt–Pd NPs decay to zero [follow the vertical arrows in Fig. 4(a)] indicates that the HE-XRD experiments conducted here are sensitive to the positioning of atoms throughout the studied NPs, including the region near their surface. That is important because the chemistry and local structure of the outermost atomic layers of metallic NPs determine their catalytic functionality to a great extent (Cuenya, 2010; Somorjai, 1994; Hammer & Nørskov, 2000).

To ascertain the overall structure type of the studied NPs, the respective experimental total atomic PDFs were approached with a simplistic model constrained to a face-centred-cubic (f.c.c.)-type lattice. The model made sense because bulk Pt, Pd, and Pt–Pd alloys are f.c.c.-type crystals (Pearson, 1972).
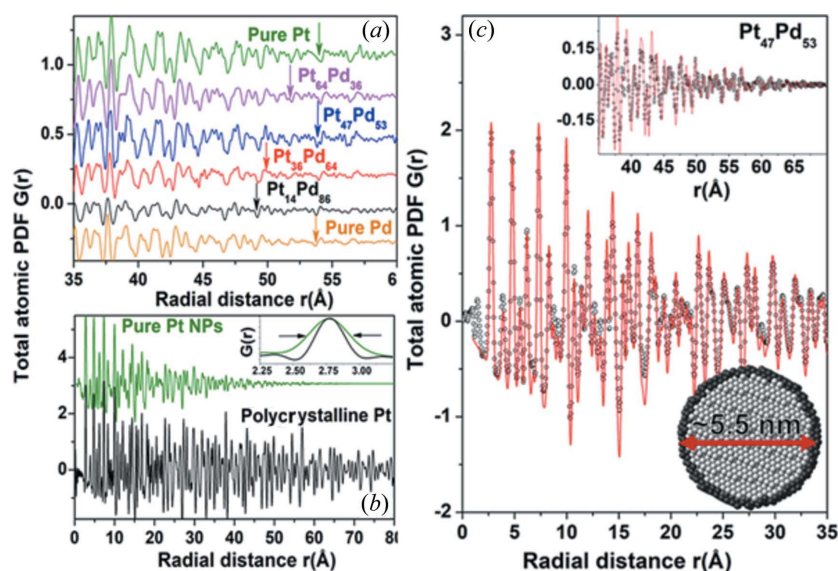
Figure 4
(a) Higher-r part of the experimental total PDFs for pure Pt, Pd and Pt_xPd_{100-x} alloy NPs (x = 14, 36, 47, 64). Vertical arrows mark the real-space distance at which the physical oscillations in the PDFs become statistically indistinguishable from the noise in the data. The distances are commensurate with the average NP size, as determined by TEM (see Fig. 1). (b) Experimental total PDFs for pure Pt NPs (green) and polycrystalline Pt (black) standard resulted from the present HE-XRD experiments. The first peak in the PDFs is shown in the inset. Horizontal arrows emphasize the increased local structural distortions in Pt NPs in comparison to bulk (polycrystalline) Pt. (c) Experimental (symbols) and computed (red line) total PDFs for pure Pt NPs. The computed PDF is derived from a three-dimensional model for 5.3 nm Pt particles refined against the experimental PDF data. The cross section of the model is shown in the lower-right corner. The darkened two outermost layers of the model comprise about 30% of all (∼7000) Pt atoms in it. Correlations between the positions of atoms forming the layers are seen as higher-r peaks in the PDF data. The peaks are shown in the inset for clarity. The observation certifies the sensitivity of atomic PDFs obtained using a point detector (Ge SSD), in particular their higher-r peaks, to the relative positioning and number of near-surface atoms in metallic NPs.

Details of the computations are given in the supporting information. Results from the computations are shown in Figs. 5(a) and 5(b). As can be seen in the figures, the NPs largely maintain the f.c.c.-type structure exhibited by their bulk counterparts. However, contrary to the case of bulk Pt–Pd alloys, the f.c.c. lattice parameter for Pt–Pd alloy NPs extracted from the experimental PDF data [red squares in Fig. 5(b)] does not obey Vegard's law, which envisions a steady linear change in the lattice parameter for continuous binary alloys, in which the two types of distinct atomic species merely substitute for one another (Gschneidner & Vineyard, 1962; Denton & Ashcroft, 1991). The observation indicates that Pt and Pd atoms in Pt–Pd alloy NPs interact and so are likely to arrange in a non-uniform manner, which is likely to affect the catalytic properties of the NPs (Cuenya, 2010; Somorjai, 1994; Hammer & Nørskov, 2000). Note that the f.c.c. lattice parameter for Pt–Pd alloy NPs obtained from the broad, Bragg-like peaks in their HE-XRD patterns [green triangles in Fig. 5(b)] obeys Vegard's law. That is largely because quantities extracted from Bragg-like peaks in diffraction patterns of metallic NPs are based on the premise that the atomic arrangement throughout the NPs is uniform. However, typically, it is not because atoms in different regions of metallic

NPs are free to arrange in low-energy configurations that are misaligned relative to each other.

An inspection of the first peak in the experimental Pt–Pt and Pd–Pd partial PDFs [see Fig. 5(d)] indicates that the average atom-to-atom bonding distance in pure Pt and Pd NPs, i.e. the size of Pt and Pd atoms constituting the NPs, is somewhat diminished compared to the bulk values of 2.755 and 2.775 Å, respectively. The effect is common to metallic NPs and attributed to finite size effects, in particular to atomic relaxation near the NP's surface (Marks, 1994; Sun, 2007; Rodriguez & Goodman, 1992). Data in Fig. 5(d) also show that, on average, the size of Pt and Pd atoms in Pt–Pd alloy NPs considerably decreases and increases, respectively, with the increase in the relative amount of Pd in the NPs. The effect is not typical for bulk Pt–Pd alloys (Pearson, 1972) and evidently appears only when Pt and Pt atoms are alloyed at the nanoscale. It can be explained on the basis of the theory of chemical bonding of Pauling, which postulates that the elemental size of metal atoms may change upon alloying so that the ratio of the size of the alloyed atoms becomes as close to one as possible, for minimizing atomic level stresses. Furthermore, the theory postulates and experiments confirm that changes in metal-to-metal atom bond lengths trigger changes in both the strength of the respective bonds and the electronic structure of the metal atoms involved in the bonds, and *vice versa*. That is, changes in the size and electronic structure of atoms in an alloy, if any, indeed occur concurrently as integral parts of the process of minimization of the alloy's energy taking place when it is formed (Pauling, 1950, 1975; Rajasekharan & Seshubai, 2012). As numerous studies have shown, changes in the size, bonding and electronic structure of alloyed noble metal atoms, including Pt and Pd atoms, would change their reactivity (Cuenya, 2010; Somorjai, 1994; Hammer & Nørskov, 2000; Quan *et al.*, 2015; Wu *et al.*, 2017). Altogether, the experimental total and element-specific PDFs appeared sensitive both to fine and to overall structural features of Pt–Pd alloy NPs that are of importance to their catalytic functionality. Hence, the PDFs were used to build realistic models for the NPs and explore the structural origin of their unusual catalytic activity for the ORR.

4. Modeling the three-dimensional atomic structure of Pt–Pd NPs

Realistic three-dimensional models for pure Pd, Pd and Pt_xPd_{100-x} alloy NPs (x = 14, 36, 47, 64) were built strictly adhering to the successful practices of structure studies by powder XRD. From a methodological point of view, this made
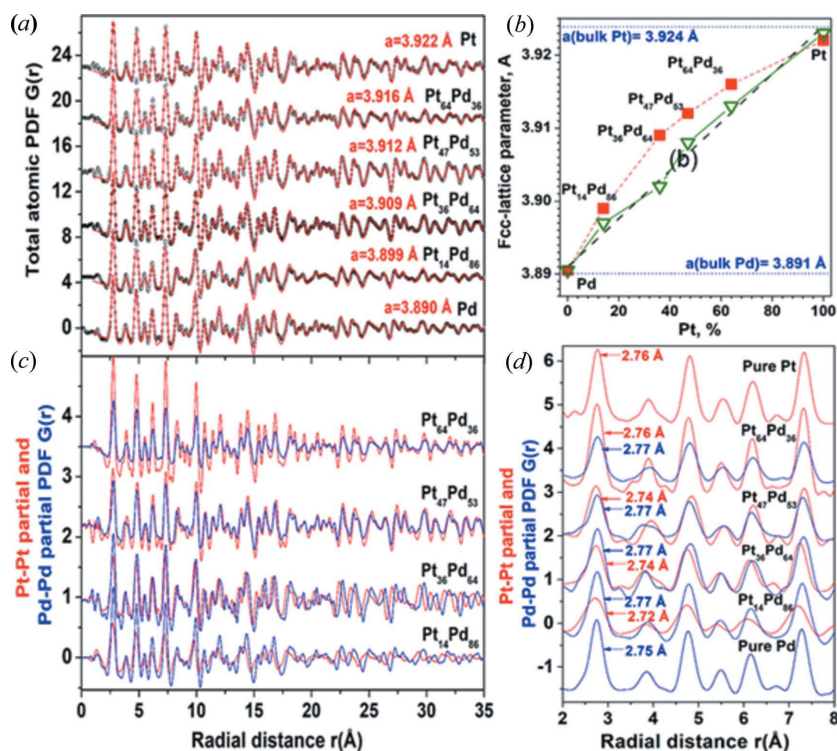
Figure 5
(a) Experimental (symbols) and computed (red line) total PDFs for pure Pt, Pd and Pt_xPd_{100-x} alloy NPs (x = 14, 36, 47, 64). The computed PDFs are based on a model constrained to an f.c.c.-type lattice as explained in the text. The refined f.c.c. lattice parameter is given for each data set. (b) Refined f.c.c. lattice parameters (red squares) from panel (a) *versus* the composition of the respective NPs. F.c.c. lattice parameters obtained from the Bragg-like peaks in the respective HE-XRD patterns (green triangles) are also shown. The red and green broken lines line through the respective data points are a guide to the eye. The diagonal broken line (in black) represents the linear (Vegard's law type) dependence of the f.c.c. lattice parameter for bulk Pt–Pd alloys on their composition, as observed by powder XRD (Pearson, 1972; Gschneidner & Vineyard, 1962). For comparison, the f.c.c. lattice parameters for bulk Pt and Pd metals are also shown. As can be seen, the f.c.c. lattice parameters derived from atomic PDFs evolve irregularly with the nanoalloy's composition whereas those derived from the respective HE-XRD patterns agree with Vegard's law. (c) Experimental Pt–Pt (red line) and Pd–Pd (blue line) partial PDFs for Pt_xPd_{100-x} alloy NPs (x = 14, 36, 47, 64). (d) Low-r part of the experimental Pt–Pt (red line) and Pd–Pd (blue line) partial PDFs for Pt_xPd_{100-x} alloy NPs (x = 14, 36, 47, 64). The low-r part of the experimental total PDFs for pure Pt (red line) and Pd (blue) NPs is also shown for comparison. The position of the first peak in the PDFs is given for each data set (follow the arrows).

based on the quantum-corrected Sutton–Chen potential (Sutton & Chen, 1990; Cagin *et al.*, 1999; Rafii-Tabar & Sulton, 1991). Example MD optimized model structures are shown in Figs. S2 and S3 in the supporting information. Details of the MD simulations can be found in the supporting information. The best MD-optimized atomic configurations were refined further by RMC computations, guided by the respective total, differential and partial atomic PDFs. The refinement was necessary since actual metallic NPs can exhibit significant surface atomic relaxation and chemical patterns that may not be captured by MD alone, *i.e.* without experimental input (Marks, 1994; Sun, 2007; Prasai *et al.*, 2015). As should be, the thermal (Debye–Waller type) and static displacements, *i.e.* relaxation, of atoms in the refined configurations were treated separately. In addition, the atoms were restrained not to come closer than pre-selected distances of closest approach and maintain as high (*i.e.* as close to 12) as possible coordination numbers, thus taking into account the close-packed (f.c.c.-type) nature of the atomic arrangement in the modeled NPs. Simultaneously, the energy of the configurations was minimized further using pair-wise potentials taken from literature sources. Details of the RMC computations are given in the supporting information. The RMC-refined three-dimensional models are shown in Fig. 6. The models have a realistic size, shape and overall chemical composition. In addition, they are optimized in terms of energy and, as demonstrated in Figs. 7 and S1 (see the supporting information), reproduce the respective total and element-specific PDF data to a very high degree. Given the excellent sensitivity of element-specific atomic PDFs to fine structural details of metallic alloy NPs, including the NP geometry and chemical pattern (see Fig. S4 in the supporting information), the three-dimensional atomic configurations shown in Fig. 6 can be considered fairly accurate. As such, and in compliance with the criteria for assessing the quality of three-dimensional atomic structures determined from powder XRD data (David *et al.*, 2002; Toby & Egami, 1992; Prasai *et al.*, 2015; Giacovazzo, 1992; Harris & Tremayne, 1996), the configurations can be considered as the most likely ensemble-averaged three-dimensional atomic structures of the NPs studied here. Therefore, the structures are fit for their purpose, that is, positions of individual Pt and Pd atoms in the structures can be used to assess the catalytic functionality of the respective NPs. Here it may be added that describing the structure of bimetallic alloys in terms of large-size atomic configurations is not a rarity. For example, the monoclinic
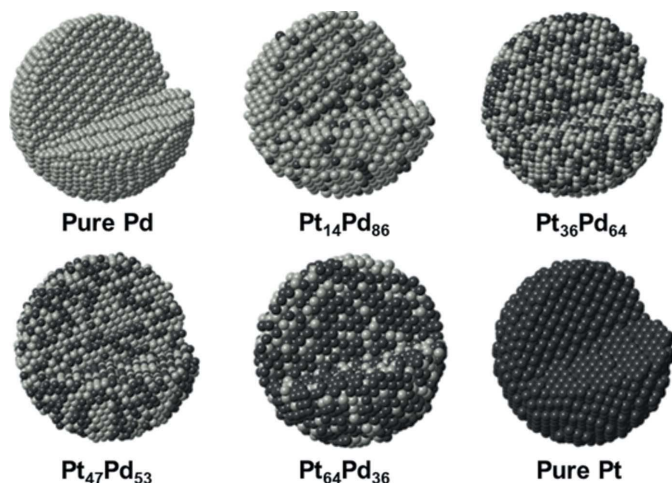
perfect sense because determining the atomic structure of both materials, appearing as fine polycrystalline powders and metallic NPs possessing a good degree of crystallinity, relies on diffraction data obtained from ensembles of entities with a close chemical composition, size and shape (David *et al.*, 2002). In brief, full-scale structures for each of the modeled NPs were generated accounting for the findings of ICP-OES, HR-TEM and EDS experiments, that is, the structures featured atomic configurations with the overall chemical composition, size (∼5.3 nm) and shape (rounded polyhedral) of the modeled NPs. Also, as suggested by the findings of crystallography-constrained analysis of the experimental total PDFs, Pt and Pd atoms (∼7000 in total) in the configurations were arranged in an f.c.c.-like manner. Configurations of various chemical patterns were considered. The energy of the configurations was minimized by molecular dynamics (MD)

Figure 6
Three-dimensional structures for pure Pt, Pd and Pt_xPd_{100-x} alloy NPs (x = 14, 36, 47, 64) obtained as described in the text. The very good agreement between the total and element-specific PDFs computed from the structures and those obtained by differential resonant HE-XRD experiments is demonstrated in Figs. 7 and S1 (see the supporting information). To reveal the mutual distribution of Pd and Pt atoms in more detail, each structure is shown with one quarter removed. Pd atoms are in gray and Pt atoms are in black.

(spacegroup $C2$) $YbCu_{4.5}$ alloy is described by a 7448-atom unit cell determined by XRD and HR-TEM (Cerný *et al.*, 1996). Then, from the point of view of traditional crystallography, Pt_xPd_{100-x} alloy NPs (x = 0, 14, 36, 47, 64, 100) can be considered as triclinic (space group $P1$) nanocrystallites described by a unit cell comprising about 7000 Pt and/or Pd atoms. The nanocrystallites though are not agglomerated in

bulk powder but are dispersed on a fine carbon support (see Fig. 1), thus becoming an integral part of a typical metal–carbon composite. This does not preclude a precise determination of their three-dimensional structure by a combination of advanced experimental and computational techniques.

5. Analysis of the three-dimensional structure models of Pt–Pd NPs

Using the (x, y, z) coordinates for Pt and Pd atoms forming the top two layers of the three-dimensional structures shown in Fig. 6, we derived structural characteristics that are directly related to the catalytic functionality of the respective NPs, such as partial surface coordination numbers (CNs) and bonding distances. Results are summarized in Figs. 8 and 9, respectively. As the data in Fig. 8(a) show, most ($\sim$70%) surface Pd and Pt atoms in Pt–Pd alloy NPs with a low Pt content, that is $Pt_{14}Pd_{86}$ NPs, have one or two Pt atoms, and from five to seven Pd atoms as first neighbors, respectively. On the other hand, most ($\sim$70%) surface Pd and Pt atoms in Pt–Pd alloy NPs with a high Pt content, that is $Pt_{64}Pd_{36}$ NPs, have from three to five Pt atoms, and from two to four Pd atoms as first neighbors, respectively. Surface Pd and Pt atoms in $Pt_{36}Pd_{64}$ and $Pt_{47}Pd_{53}$ alloy NPs have nearly the same number of unlike near neighbors. This observation indicates that surface Pd and Pt atoms in Pt–Pd alloy NPs studied here are well intermixed together. The distribution of partial surface CNs for hypothetical Pt–Pd random-alloy NPs with the same size, shape and overall chemical compositions is shown in Fig. 8(b). A comparison between data in Figs. 8(a) and 8(b) indicates that the mutual distribution of surface Pd and Pt atoms in the actual Pt–Pd NPs is not quite random. In particular, the number of Pd and Pt monomers in $Pt_{14}Pd_{86}$ and $Pt_{64}Pd_{36}$ alloy NPs, respectively, appears reduced compared to that in their random-alloy counterparts. Evidently, because of their interaction, surface Pd and Pt atoms in the Pt–Pd alloy NPs studied here exhibit a preference for unlike near neighbors.

The distribution of surface Pd—Pd and Pt—Pt bonding distances in pure Pt, Pd and Pt–Pd alloy NPs is shown in Figs. 9(a) and 9(b), respectively. As the data in the figures show, on average, surface Pd—Pd and Pt—Pt distances in pure Pd and Pt NPs are somewhat shorter than the respective bulk values (2.748 Å for the NPs *versus* 2.755 Å for bulk Pd, and 2.758 Å for the NPs *versus* 2.775 Å for bulk Pt). Such a shortening is common for metallic NPs and attributed to finite size effects (Marks, 1994; Sun, 2007). Data also show that, on average, the length of surface Pt—Pt distances in Pt–Pd alloy NPs decreases further with the Pd content, reaching a value 2.717 Å when that content approaches 86%. On the other hand, on average, the length of surface Pd—Pd
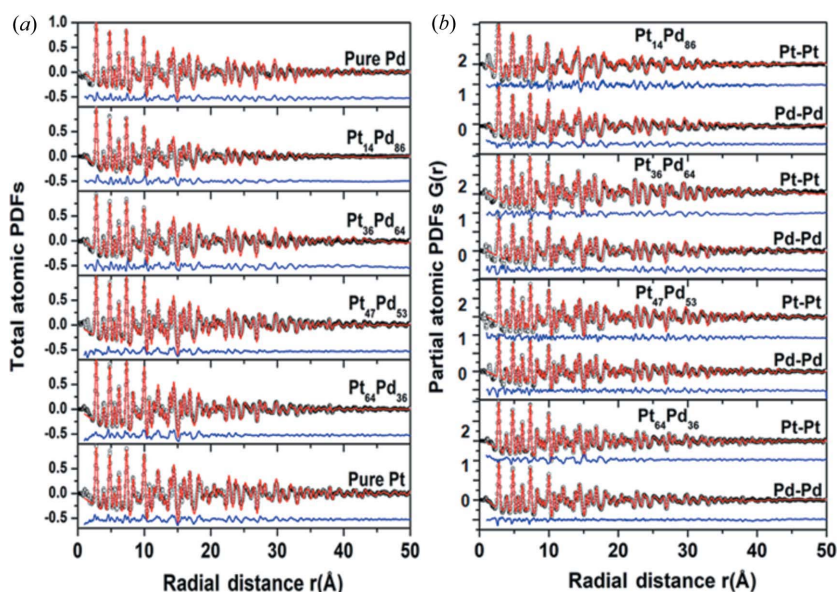

Figure 7
(a) RMC fits (red lines) to the experimental (symbols) total PDFs for pure Pt, Pd and Pt_xPd_{100-x} alloy NPs (x = 14, 36, 47, 64). (b) RMC fits (red lines) to the experimental (symbols) Pt–Pt and Pd–Pd partial PDFs for the NPs. The fits reflect the respective three-dimensional structures shown in Fig. 6. The residual difference (blue line) between the experimental and RMC-fit PDFs is given for each data set shifted by a constant factor for clarity. The goodness-of-fit indicators R_w, defined in the supporting information, for the RMC fits are of the order of 11–15%.
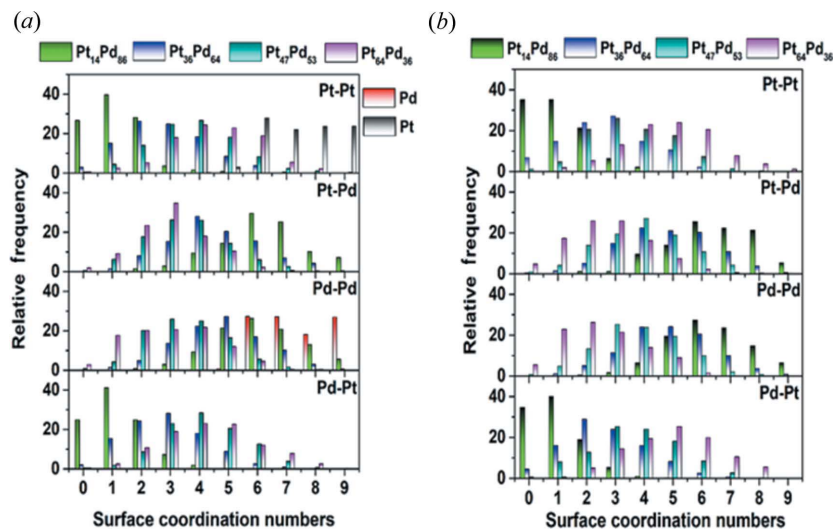
(a)

(b)

Figure 8
(a) Distribution of partial coordination numbers (CNs) for surface atoms in Pt_xPd_{100-x} alloy NPs (x = 14, 36, 47, 64) studied here and (b) hypothetical Pt–Pd random-alloy NPs with the same size, shape and chemical composition. Data in (a) are extracted from the respective three-dimensional model structures shown in Fig. 6. Note that the CN for surface atoms occupying the (111) facet of bulk Pt/Pd is 9.

distances increases with the Pt content in the NPs, reaching a value 2.769 Å when that content approaches 64%. The observed systematic change in the bonding distances between like surface atoms in Pt–Pd alloy NPs by nearly reciprocal factors is not exhibited by bulk Pt–Pd alloys. Apparently, it is the origin of the irregular evolution of the f.c.c. lattice parameter of the former compared to that of the latter [see Fig. 5(b)]. As discussed above, concurrent systematic changes in the distances between nearby atoms at the surface of

(a)

(b)

Figure 9
Distribution of surface (a) Pd—Pd and (b) Pt—Pt bonding distances (red bars) in pure Pt, Pd and Pt_xPd_{100-x} alloy NPs (x = 14, 36, 47, 64). Solid red lines are Gaussian functions fitted to the distributions. The centroid of the distributions, i.e. the average surface Pd—Pd and Pt—Pt bonding distances, are shown for each data set. Vertical broken lines (in blue) mark Pd—Pd and Pt—Pt bonding distances in bulk Pd and Pt metals. Data are extracted from the respective three-dimensional model structures shown in Fig. 6.

metallic NPs, usually referred to as surface atomic relaxation, would affect the distribution of the electron density at the NP surface considerably. Here it is to be stressed that resonant HE-XRD is very suitable for studying changes in the surface electronic structure of metallic NPs, including Pt–Pd alloy NPs, because X-rays are scattered by the electron cloud surrounding the nuclei of metal atoms and, furthermore, the near-surface region of metallic NPs incorporates a very substantial fraction of all atoms in the NPs. In addition, element-specific atomic PDFs resulting from resonant HE-XRD experiments reflect X-ray intensities collected over a broad range of wavevectors (in our case, from $q_{min} \simeq 1$ Å^{-1} to $q_{max} \simeq 25$ Å^{-1}). This renders them sensitive both to the valence (the major contributor to X-ray intensities collected at relatively low q values) and the tightly bound (the major contributor to X-ray intensities collected at relatively high q values) electrons of metal atoms, including Pt and Pd. For reference, the valence electron configuration of Pt (Z = 78) and Pd (Z = 46) atoms in the respective metals is $5d^{8.66}6(sp)^{1.34}$ and $4d^{9.4}5(sp)^{0.6}$. Extra sensitivity to the electronic structure of Pt and Pd atoms is achieved by probing their K edge, thereby exciting their tightly bound electrons.

Generally, the size of a metal atom can be considered in terms of its elemental Wigner–Seitz radius, r_{ws}, defined as the radius of a sphere whose volume, V_{ws}, is equal to the volume of the Wigner–Seitz (WS) cell occupied by the atom in the respective bulk metal. In the case of N metal atoms in a volume V of the metal, the Wigner–Seitz radius can be defined as $(4/3)\pi(r_{ws})^3 = V/N$. Solving for r_{ws}, it can be obtained that $r_{ws} = \{3/[4\pi n(r)]\}^{1/3}$, where $n(r)$ is the average valence electron density of the atom (Pauling, 1950, 1975; Ashcroft & Mermin, 1976). Therefore, locally, the size of a metal atom can be related to the spatial extent of the highest-energy occupied (outermost) valence electron orbitals of the atom (Watson et al., 1971; Straub & Harrison, 1985; Coulthard & Sham, 1996). Then, within the formalism of WS cells, it may be considered that the further 'compressed' and 'expanded' surface Pt and Pd atoms in Pt–Pd alloy NPs have lost and gained electrons occupying their outermost orbitals, respectively. In particular, considering the observed decrease in the surface Pt—Pt bonding distances and related strengthening of d–d electron interactions, it may be surmised that 'compressed' surface Pt atoms have lost electrons of 6sp character through $6sp \rightarrow 5d$ charge redistribution and so their valence electronic configuration
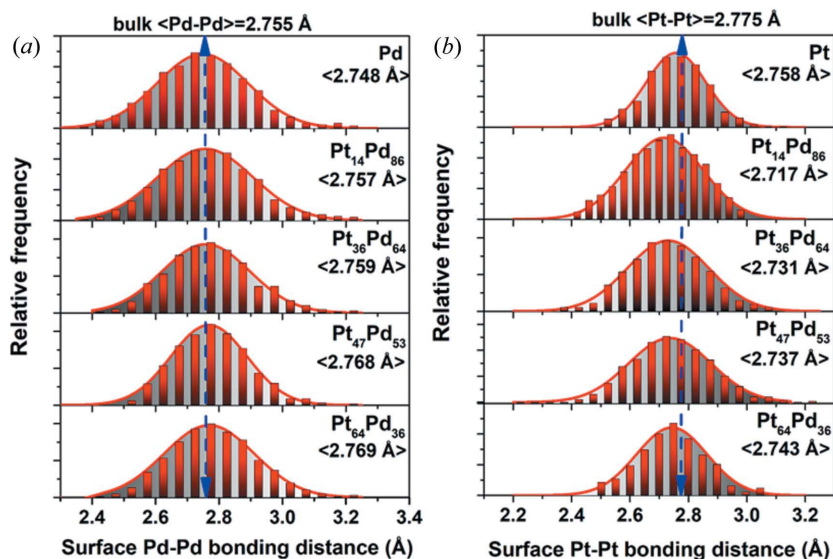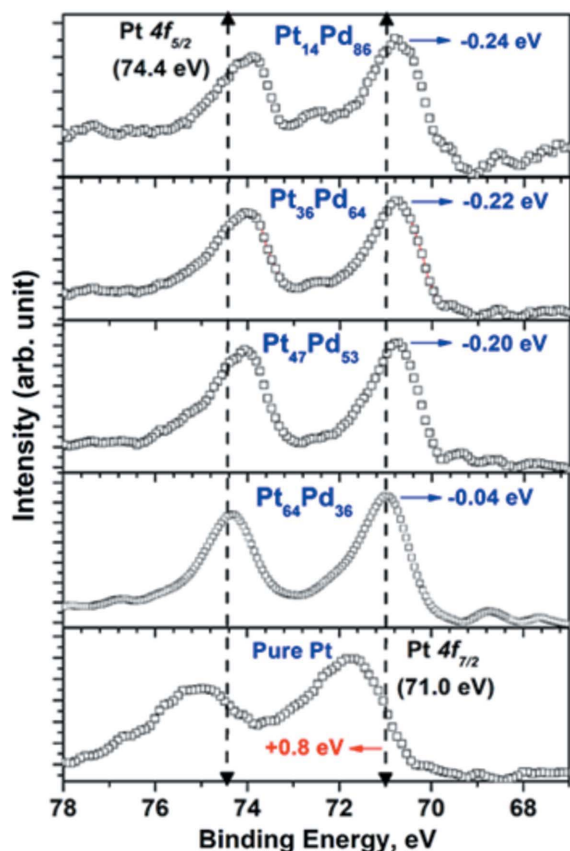
Figure 10
Typical XPS Pt $4f_{7/2}$ spectra for pure Pt and Pt_xPd_{100-x} alloy NPs ($x = 14$, 36, 47, 64). The shift of the binding energy of Pt atoms in the respective NPs are evaluated (arrows) with respect to the Pt $4f_{7/2}$ (71.0 eV) line (vertical broken line) characteristic to bulk Pt metal.

becomes more $5d^{10}6s^1$-like [*versus* the $5d^{9.6}6(sp)^{1.4}$ bulk configuration]. Effectively, the increased population of $5d$ orbitals and decreased (d-orbital)–(d-orbital) separation (because of the decreased Pt—Pt bonding distances) would push the center of gravity, *i.e.* average energy position, of the valence d band of 'compressed' surface Pt atoms downward with respect to the Fermi level in the NPs. To validate our findings, we investigated the electronic properties of near-surface Pt atoms in Pt–Pd NPs by XPS. Details of the XPS experiments are given in the supporting information. Typical Pt $4f$ spectra are shown in Fig. 10. As can be seen in the figure, and in line with the work of others (Knecht *et al.*, 2008), the Pt $4f_{7/2}$ core-level peak position in pure Pt NPs is shifted to a higher energy (+0.8 eV) with respect to the bulk value of 71.0 eV. On the other hand, the Pt $4f_{7/2}$ core-level peak position in $Pt_{14}Pd_{96}$, $Pt_{36}Pd_{64}$, $Pt_{47}Pd_{53}$ and $Pt_{64}Pd_{36}$ alloy NPs appears shifted to a lower energy by −0.24, −0.22, −0.20 and −0.04 eV, respectively. The observed systematic shift of the inner-core orbitals of surface Pt atoms in Pt–Pd alloy NPs to a lower energy indicates that the population of their valence d band increases with the decrease in their relative percentage, which is likely to be caused by interactions with nearby surface Pd atoms (Xue & Guo, 2012; Toda *et al.*, 1999). The observation provides strong evidence in support of the findings of our structure study on Pt–Pd alloy NPs, in particular the

observed systematic shortening of Pt—Pt bonding distances. On the other hand, considering the observed increase in Pd—Pd bonding distances and related weakening of d–d electron interactions, it may be surmised that 'expanded' surface Pd atoms have lost electrons of $4d$ character through $4d \rightarrow 5sp$ charge redistribution and so their valence electrons gained some more $5sp$ character, which is likely to be caused by interactions with nearby surface Pt atoms. Effectively, the decreased d-orbital population and increased (d-orbital)–(d-orbital) separation (because of the increased Pd—Pd bonding distances) would narrow the $4d$ band of 'expanded' surface Pd atoms, pushing its top below the Fermi level in the NPs. The effect will be particularly strong with $Pt_{64}Pd_{36}$ alloy NPs wherein, on average, surface Pd atoms appear markedly 'expanded' in comparison with corresponding surface atoms in pure Pd NPs [see Fig. 9(a)]. The concurrent changes in the valence-electron structure of surface Pt and Pd atoms in Pt–Pd alloy NPs may also be considered in terms of a subtle transfer of sp charge from the former to the latter and back-transfer of d charge in return, to maintain local electroneutrality. The net change in the surface electronic structure of the NPs though would be the same. Regardless of the underlying mechanism, changes in the surface electronic structure may be expected to alter the binding energy of gas-phase species to the surface of Pt–Pd alloy NPs in comparison to pure Pt and Pd NPs. Accordingly, the ORR activity of the NPs studied here may be expected to vary with their chemical composition (Cuenya, 2010; Somorjai, 1994; Hammer & Nørskov, 2000).

6. Three-dimensional structure–catalytic functionality relationship for Pt–Pd NPs

Without loss of generality, the ORR over a catalyst surface can be expressed as $O_2 + 4H^+ + 4e^- \rightarrow H_2O$. That is, oxygen molecules adsorbed and reduced at the surface react with protons supplied to the surface to form water. Though the exact mechanism of the ORR over different catalysts is still under debate, there is strong experimental evidence that the reaction proceeds *via* a number of elementary steps. Among others, the steps involve a cleavage of the strong O—O bond in molecular oxygen adsorbed on the catalyst surface and removal of reaction intermediates such as *OH and *OOH groups leading to the formation of water. Here '*' represents an active surface site capable of binding ORR reactants and reaction intermediates. Generally, it is considered that an efficient catalyst for the ORR would bind oxygen molecules with ample strength to allow the cleavage of O—O bonds and formation of OH/OOH groups but weakly enough to liberate the latter through producing water when the reaction is complete. In addition, it is believed that the binding energy of atomic oxygen can serve as an indicator for catalytic activity for the ORR (Cuenya, 2010; Nørskov *et al.*, 2004; Sepa *et al.*, 1981). Pt is the best monometallic catalyst for ORR, even though, according to theory, it binds oxygen a bit too strongly by about 0.2 eV. Pd is even more reactive toward oxygen species in comparison to Pt. Our data for the specific (SA) and mass (MA) catalytic activity of pure Pt, Pd and Pt–Pd alloy
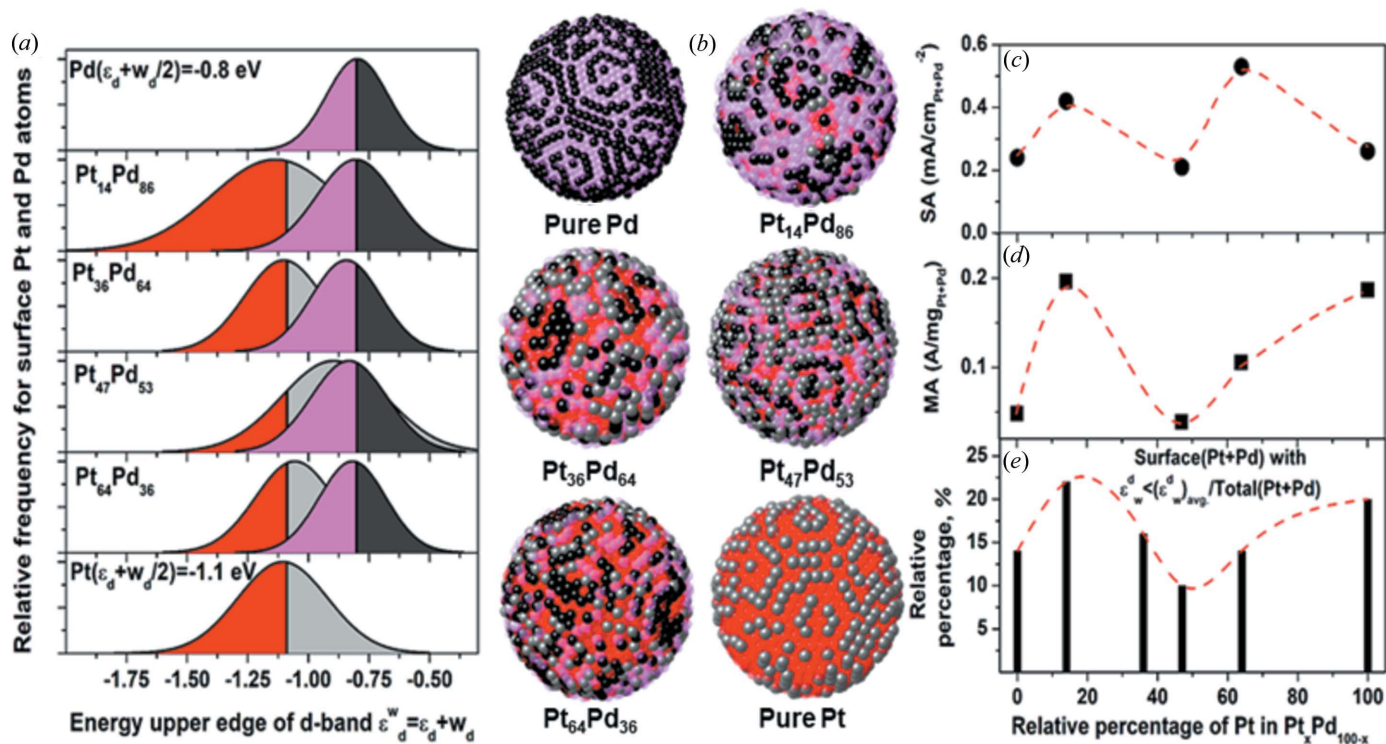
Figure 11
(a) Distribution of the energy of the upper edge of the valence d band, $\varepsilon_w^d = (\varepsilon_d + w_{d/2})$, for surface Pt (red and gray) and Pd (magenta and black) atoms in pure Pt, Pd and Pt_xPd_{100-x} alloy NPs (x = 14, 36, 47, 64). The average value of ε_w^d for surface Pt ($\varepsilon_w^d = -1.1$ eV) and Pd atoms ($\varepsilon_w^d = -0.8$ eV) in pure Pt and Pd NPs is also shown. It is used to partition the respective distributions as follows: the part of a distribution falling below the average value of the respective ε_w^d is colored in either red (for Pt) or magenta (for Pd). The part of a distribution appearing above the average value of the respective ε_w^d is colored in either gray (for Pt) or black (for Pd). (b) Maps of the NP surface where each Pt and Pd atom is colored according to the value of ε_w^d for the atom. Colors, and their meaning, correspond to those used in (a). (c) Specific activity (circles) of standard E-tek/Pt, E-tek/Pd and Pt_xPd_{100-x} alloy NPs (x = 14, 47, 64) for the oxygen reduction reaction (ORR). The broken red line is a guide to the eye. (d) Mass activity (squares) of standard E-tek/Pt, E-tek/Pd and Pt_xPd_{100-x} alloy NPs (x = 14, 47, 64) for the ORR. The broken red line is a guide to the eye. (e) Relative percentage of surface Pt and Pd atoms whose ε_w^d falls in the left-hand side of the distributions shown in (a) versus the total number (Pt + Pd) atoms in the respective NPs. The broken red line is a guide to the eye. Note that data in (c) and (d) are also normalized against the total amount of noble metal (Pt + Pd) used in the respective system of NPs. Also, it is to be noted that results presented in the figure lend support to the validity of ε_w^d as a descriptor for the reactivity of transition metal surfaces.

NPs for the ORR are shown in Figs. 11(c) and 11(d), respectively. The data were obtained by standard cyclic voltametry and rotating disk electrode experiments described in the supporting information. In line with the work of others, the data in the figures show that Pt–Pd alloy NPs are very promising catalysts for the ORR (Lu et al., 2013; Quan et al., 2015; Li et al., 2007; Wu et al., 2017). Their ORR activity though exhibits a hard-to-comprehend evolution with their composition, making it difficult to design a strategy for optimizing the former by adjusting the latter.

Qualitatively, the improvement in the ORR activity of Pt–Pd alloy NPs can be attributed to one or more of the following factors: (i) ligand/electronic effects arising from charge exchange between surface Pt and Pd atoms (i.e. heteroatom interactions), (ii) strain effects arising from the difference between the size of Pt and Pd atoms, and (iii) geometric effects where particular configurations of surface Pt and Pd atoms appear beneficial to the ORR (Cuenya, 2010; Somorjai, 1994; Hammer & Nørskov, 2000). As the results of three-dimensional structure modeling and complementary XPS experiments indicate, the energy position, ε_d, and

population of the valence d band of surface Pt and Pd atoms in the NPs, often referred to as the d-electron density of states (d-DOS), change with their composition. As theory predicts, the changes, in particular the interrelated diminishing of the d-DOS and downshift of ε_d for surface Pt and Pd sites with respect to the Fermi level, would reduce the reactivity of Pt–Pd alloy NPs toward oxygen and oxygenated species (*OH/*OOH), thereby improving their SA for the ORR in comparison to pure Pt and Pd NPs (Hammer & Nørskov, 2000; Kitchin et al., 2004b; Xin et al., 2014). To understand the oscillatory evolution of the SA and MA of Pt–Pd alloy NPs for the ORR with their compositions, we computed the energy position of the upper edge of the d band, ε_w^d, of all surface Pt and Pd atoms in the NPs using the positions of surface atoms in the respective three-dimensional structure models. According to the modified d-band center theory on the catalytic properties of transition metals and their alloys, ε_w^d correlates with the binding energy of oxygen species adsorbed on surface Pt and Pd sites and so can be used as a descriptor of their reactivity (Xin et al., 2014; İnoğlu & Kitchin, 2010; Vojvodic et al., 2014). Details of the computations are given in

the supporting information. Results of the computations are summarized in Fig. 11(a). As can be seen in the figure, computed ε_w^d values show broad distributions reflecting the diversity of atomic sites at the surface of the respective NPs. Color maps indicative of the reactivity of the surface of Pt_xPd_{100-x} alloy NPs ($x = 0, 14, 36, 47, 64, 100$) towards oxygen species are shown in Fig. 11(b). Surface Pt atoms whose ε_w^d is lower and higher than the average ε_w^d value for surface Pt sites in pure Pt NPs (-1.1 eV) are given in red and gray, respectively. Surface atoms Pd atoms whose ε_w^d is lower and higher than the average ε_w^d value for surface Pd sites in pure Pd NPs (-0.8 eV) are given in magenta and black, respectively. Thus, brighter colors (magenta and red) indicate surface sites that, according to the ε_w^d descriptor for reactivity, would promote the ORR. The sites are seen to involve largely planar-type atomic configurations that are believed to be more active catalytically for the ORR than sharp edges and vertices at the NP surface. The observation indicates that both geometric and electronic effects in Pt–Pd alloy NPs, arising from interaction between nearby surface Pt and Pd atoms, may be equally important to their performance as catalysts for the ORR. The latter though are intimately coupled with the observed irregular change in the surface Pt—Pt and Pd—Pd bonding distances (strain effects) and not quite random-alloy character of the NPs. Remarkably, when normalized against the total number of Pt and Pd atoms in the respective NPs, the percentage of surface Pt and Pd atoms with a reduced ε_w^d closely tracks the observed oscillatory evolution of the ORR activity of the NPs with their composition [see Fig. 11(e)]. Altogether, experimental catalytic, atomic and computed electronic structure data (compare the respective data sets in Figs. 9, 10 and 11) strongly indicate that Pt–Pd alloy NPs with low Pt content, wherein surface Pt atoms are considerably 'compressed' and isolated from each other ($CN_{Pt-Pt} \leq 1$) and, at the same time, surface Pd atoms are moderately 'expanded' and have up to two Pt neighbors ($CN_{Pd-Pt} \leq 2$), are likely to outperform other Pt–Pd catalysts for ORR. Currently, our effort to produce Pt–Pd nanoalloy catalysts with highly improved ORR activity follows the clues provided by the present structure study. Here is to be added that the catalytic synergy between Pt and Pd atoms in Pt–Pd nanoalloys would have been difficult to reveal if the nanoalloys had been considered as random-type solid solutions, as suggested by the traditional analysis of the Bragg-like peaks in their HE-XRD patterns.

7. Conclusion

The contribution of the surface and interior of materials confined to nanosized dimensions to their physicochemical properties can differ significantly. Often, the former overwhelms the latter, thereby endowing the materials with unique functionalities. This is largely because the atomic arrangement in nanosized materials defies the laws of traditional crystallography. To harness the functionalities though, precise knowledge of the inherently non-periodic atomic structure of nanosized materials is needed. As demonstrated here using Pt–Pd alloy NPs as an example, differential resonant HE-XRD coupled to element-specific atomic PDFs analysis can greatly facilitate determining the three-dimensional atomic arrangement in nanosized materials by providing structure data with both excellent spatial resolution and element specificity. Differential resonant HE-XRD experiments can be conducted at the K edge of one or more pre-selected species in nanosized materials with the goal of obtaining differential and/or partial PDFs and so reveal the atomic correlations involving the species in better detail. When augmented with structure-sensitive information delivered by complementary techniques and integrated with advanced computational procedures, total and element-specific PDFs can guide three-dimensional structure modeling of nanosized materials, including determining the positions of individual atoms. From the positions, physicochemical properties deemed important for practical applications can be assessed and so the structure–function relationship for the studied nanosized materials can be clarified. The knowledge can provide a sound atomic-level basis for developing of better nanosized materials by rational design. It can also provide a feedback loop for streamlining their synthesis and optimization for practical applications. Given this, and the number of high-energy synchrotron radiation facilities available worldwide, the technique can find widespread utility.

8. Related literature

The following articles are cited in the supporting information: Cargill (1971); Gereben & Petkov (2013); Jensen *et al.* (2016); Jiang *et al.* (2009); Kitchin *et al.* (2004a); Kodama *et al.* (2006); McGreevy & Pusztai (1988); Olds *et al.* (2015); Petkov *et al.* (2014); Skinner *et al.* (2013); Smith *et al.* (2002); Warren (1969); Zhen & Davies (1983).

References

Ashcroft, N. W. & Mermin, N. D. (1976). *Solid State Physics.* New York: Harcourt College Publishers.
Billinge, S. J. L. & Levin, I. (2007). *Science*, **316**, 561–565.
Cagin, T., Qi, Y., Li, H., Kimura, Y., Ikeda, H., Johnson, W. L. & Goddard, W. A. III (1999). *MRS Symp. Ser.* **554**, 43–48.
Callister, W. D. (2007). *Materials Science and Engineering: An Introduction*, 7th ed. New York: Wiley.
Cargill, G. S. (1971). *J. Appl. Cryst.* **4**, 277–283.

Cerný, R., François, M., Yvon, K., Jaccard, D., Walker, E., Petrícek, V., Císarová, I., Nissen, H. & Wessicken, R. (1996). *J. Phys. Condens. Matter*, **8**, 4485–4493.

Chantler, C. T. (1995). *J. Phys. Chem. Ref. Data*, **24**, 71–643.

Coulthard, I. & Sham, T. K. (1996). *Phys. Rev. Lett.* **77**, 4824–4827.

Cuenya, B. R. (2010). *Thin Solid Films*, **518**, 3127–3150.

David, W. I. F., Shakland, K., McCusker, L. B. & Baerlocher, C. (2002). *Structure Determination from Powder Diffraction*. IUCr Monographs on Crystallography 13. Oxford University Press.

Denton, A. R. & Ashcroft, N. W. (1991). *Phys. Rev. A*, **43**, 3161–3164.

Egami, T. & Billinge, S. J. L. (2003). *Underneath the Bragg Peaks: Structural Analysis of Complex Materials*, 1st ed. New York: Pergamon Press.

Evans, R. F. L., Chantrell, R. W. & Chubykalo-Fesenko, O. (2013). *MRS Bull.* **38**, 909–914.

Farrow, L., Juhas, P. J., Liu, J. W., Bryndin, D., Božin, E., Bloch, J., Proffen, Th. & Billinge, S. J. L. (2007). *J. Phys. Condens. Matter*, **19**, 335219.

Farrow, C., Shaw, M., Kim, H., Juhás, P. & Billinge, S. J. L. (2011). *Phys. Rev. B*, **84**, 134105.

Fuoss, P. H., Eisenberger, P., Warburton, W. K. & Bienenstock, A. (1981). *Phys. Rev. Lett.* **46**, 1537–1540.

Gereben, O. & Petkov, V. (2013). *J. Phys. Condens. Matter*, **25**, 454211–9.

Giacovazzo, C. *et al.* (1992). *Fundamentals of Crystallography*. IUCr Texts on Crystallography 2. Oxford University Press.

Gschneidner, K. A. Jr & Vineyard, G. H. (1962). *J. Appl. Phys.* **33**, 3444–3450.

Hammer, B. & Nørskov, J. K. (2000). *Adv. Catal.* **45**, 71–129.

Harris, K. D. M. & Tremayne, M. (1996). *Chem. Mater.* **8**, 2554–2570.

Huang, W. J., Sun, R., Tao, J., Menard, L. D., Nuzzo, R. G. & Zuo, J. M. (2008). *Nat. Mater.* **7**, 308–313.

İnoğlu, N. & Kitchin, J. R. (2010). *Mol. Simul.* **36**, 633–638.

Jensen, K. M. Ø., Juhás, P., Tofanelli, M. A., Heinecke, C. L., Vaughan, G., Ackerson, C. J. & Billinge, S. J. L. (2016). *Nat. Commun.* **7**, 11859.

Jiang, T., Mowbray, D. J., Dobrin, S., Falsig, H., Bligaard, T. & Nørskov, J. K. (2009). *J. Phys. Chem.* **113**, 10548–10553.

Kitchin, J. R., Nørskov, J. K., Barteau, M. A. & Chen, J. G. (2004a). *J. Chem. Phys.* **120**, 10240–10246.

Kitchin, J. R., Nørskov, J. K., Barteau, M. A. & Chen, J. G. (2004b). *Phys. Rev. Lett.* **93**, 156801.

Klug, P. K. & Alexander, L. E. (1974). *X-ray Diffraction Procedures: For Polycrystalline and Amorphous Materials*, 2nd ed. New York: Wiley-Interscience.

Knecht, M. R., Weir, M. G., Myers, V. S., Pyrz, W. D., Ye, H., Petkov, V., Buttrey, D. J., Frenkel, A. I. & Crooks, R. M. (2008). *Chem. Mater.* **20**, 5218–5228.

Kodama, K., Iikubo, S., Taguchi, T. & Shamoto, S. (2006). *Acta Cryst.* A**62**, 444–453.

Kofalt, D. D., Nanao, S., Egami, T., Wong, K. M. & Poon, S. J. (1986). *Phys. Rev. Lett.* **57**, 114–117.

Kortright, B. & Bienenstock, A. (1988). *Phys. Rev. B*, **37**, 2979–2996.

Li, H. Q., Sun, G. Q., Li, N., Sun, S., Su, D. S. & Xin, Q. (2007). *J. Phys. Chem. C*, **111**, 5605–5617.

Lin, C.-A., Lee, C.-H., Hsiech, J.-T., Wang, H. H., Li, J. K., Shen, J. L., Chan, W. H., Yeh, H.-I. & Chang, W. H. (2009). *Jpn. J. Med. Electron. Biol. Eng.* **29**, 276–283.

Link, S., Wang, Z. L. & El-Sayed, M. A. (1999). *J. Phys. Chem. B*, **103**, 3529–3533.

Lu, Y. Z., Jiang, Y. Y. & Chen, W. (2013). *Nano Energy*, **2**, 836–844.

Marks, D. (1994). *Rep. Prog. Phys.* **57**, 603–649.

Matsubara, E. & Waseda, Y. (1986). *Sci. Rep. RITU*, **33**, 1–14.

McGreevy, R. L. & Pusztai, L. (1988). *Mol. Simul.* **1**, 359–367.

Munro, G. R. (1982). *Phys. Rev. B*, **25**, 5037–5045.

Nørskov, J. K., Rossmeisl, J., Logadottir, A., Lindqvist, L., Kitchin, J. R., Bligaard, T. & Jónsson, H. (2004). *J. Phys. Chem. B*, **108**, 17886–17892.

Olds, D., Wang, H.-W. & Page, K. (2015). *J. Appl. Cryst.* **48**, 1651–1659.

Pauling, L. (1950). *Proc. Natl Acad. Sci. USA*, **36**, 533–538.

Pauling, L. (1975). *The Nature of the Chemical Bond and the Structure of Molecules and Crystals*. Ithaca: Cornell University Press.

Pearson, W. B. (1972). *The Crystal Chemistry and Physics of Metals and Alloys*. New York: Wiley-Interscience.

Petkov, V. (2008). *Mater. Today*, **11**, 28–38.

Petkov, V., Billinge, S. J. L., Shastri, S. D. & Himmel, B. (2000). *Phys. Rev. Lett.* **85**, 3436–3439.

Petkov, V., Prasai, B., Ren, Y., Shan, S., Luo, J., Joseph, P. & Zhong, C.-J. (2014). *Nanoscale*, **6**, 10048–10061.

Petkov, V., Prasai, B., Shastri, S. D., Park, H.-U., Kwon, Y.-U. & Skumryev, V. (2017). *Nanoscale*, **9**, 15505–15514.

Petkov, V. & Shastri, S. D. (2010). *Phys. Rev. B*, **81**, 165428.

Prasai, B., Wilson, A. R., Wiley, B. J., Ren, Y. & Petkov, V. (2015). *Nanoscale*, **7**, 17902–17922.

Quan, X. C., Mei, Y., Xu, H. D., Sun, B. & Zhang, X. (2015). *Electrochim. Acta*, **165**, 72–77.

Rafii-Tabar, H. & Sulton, A. S. (1991). *Philos. Mag. Lett.* **63**, 217–224.

Rajasekharan, T. & Seshubai, V. (2012). *Acta Cryst.* A**68**, 156–165.

Rodriguez, J. A. & Goodman, D. W. (1992). *Science*, **257**, 897–903.

Ruland, W. (1964). *Br. J. Appl. Phys.* **15**, 1301–1307.

Seh, Z., Kibsgaard, J., Dickens, C. F., Chorkendorff, I., Nørskov, J. K. & Jaramillo, T. F. (2017). *Science*, **355**, eaad4998.

Sepa, D. B., Vojnovic, M. V. & Damjanovic, A. (1981). *Electrochim. Acta*, **26**, 781–793.

Serimaa, R., Serimaa, O. & Bienenstock, A. (1995). *J. Non-Cryst. Solids*, **192&193**, 372–375.

Shastri, S. D. (2004). *J. Synchrotron Rad.* **11**, 150–156.

Shevchik, N. J. (1977a). *Philos. Mag.* **35**, 805–809.

Shevchik, N. J. (1977b). *Philos. Mag.* **35**, 1289–1298.

Skinner, L. B., Huang, C., Schlesinger, D., Pettersson, L. G. M., Nilsson, A. & Benmore, C. J. (2013). *J. Chem. Phys.* **138**, 074506–12.

Smith, W., Yong, W. C. & Rodger, P. M. (2002). *Mol. Simul.* **28**, 385–471.

Somorjai, G. A. (1994). *Introduction to Surface Chemistry and Catalysis*. New York: Wiley.

Straub, G. K. & Harrison, W. A. (1985). *Phys. Rev. B*, **31**, 7668–7679.

Sun, S. G. (2007). *Prog. Solid State Chem.* **35**, 1–159.

Sutton, A. P. & Chen, J. (1990). *Philos. Mag. Lett.* **61**, 139–146.

Tartaj, P., Morales, M. D. P., Veintemillas-Verdaguer, S., González-Carreño, T. & Serna, C. J. (2003). *J. Phys. D Appl. Phys.* **36**, R182–R197.

Tian, N., Zhou, Z. & Sun, S. (2008). *J. Phys. Chem. C*, **112**, 19801–19817.

Toby, B. H. & Egami, T. (1992). *Acta Cryst.* A**48**, 336–346.

Toda, T., Igarashi, H., Ucida, H. & Watanabe, M. (1999). *J. Electrochem. Soc.* **146**, 3750–3756.

Vojvodic, A., Nørskov, J. K. & Abild-Pedersen, F. (2014). *Top. Catal.* **57**, 25–32.

Wang, Z. L., Gao, R. P., Nikoobakht, B. & El-Sayed, M. A. (2000). *J. Phys. Chem. B*, **104**, 5417–5420.

Warren, B. E. (1969). *X-ray Diffraction*. Reading: Addison-Wesley.

Waseda, Y. (1984). *Novel Applications of Anomalous (Resonance) X-ray Scattering for Characterization of Disordered Materials*. Berlin: Springer.

Watson, R. E., Hudis, J. & Perlman, M. L. (1971). *Phys. Rev. B*, **4**, 4139–4144.

Wu, J., Shan, Sh., Cronk, H., Chang, F., Kareem, H., Zhao, Y., Luo, J., Petkov, P. & Zhong, Ch.-J. (2017). *J. Phys. Chem. C*, **121**, 14128–14136.

Wurden, C., Page, K., Llobet, A., White, C. E. & Proffen, Th. (2010). *J. Appl. Cryst.* **43**, 635–638.

Xin, H., Vojvodic, A., Voss, J., Nørskov, J. K. & Abild-Pedersen, F. (2014). *Phys. Rev. B*, **89**, 115114–5.

Xue, M. & Guo, Q. (2012). *Chem. Phys. Lett.* **551**, 92–95.

Zhen, S. & Davies, G. J. (1983). *Phys. Status Solidi A*, **78**, 595–605.